PERGAMON

International Journal of Solids and Structures 40 (2003) 5539–5564

INTERNATIONAL JOURNAL OF SOLIDS and STRUCTURES

www.elsevier.com/locate/ijsolstr

A general failure criterion for spot welds under combined loading conditions

S.-H. Lin [a], J. Pan [a,*], T. Tyan [b], P. Prasad [b]

[a] *Mechanical Engineering, 2250 GGB Building, The University of Michigan, Ann Arbor, MI 481092125, USA*
[b] *Ford Motor Company, Dearborn, MI 48121, USA*

Received 5 June 2003; received in revised form 11 June 2003

Abstract

The circumferential failure mode of spot welds is investigated under combined loading conditions. Failure mechanisms of spot welds under different loading conditions are first examined by the experimental observations and a plane stress finite element analysis. An approximate limit load analysis for spot welds is then conducted to understand the failure loads of spot welds under combinations of resultant forces and resultant moments with consideration of the global equilibrium conditions only. The approximate limit load solution for circumferential failure is expressed in terms of sheet thickness, nugget diameter and combinations of loads. Failure contours are generated for spot welds under opening and shear loading conditions. The results indicate that failure contours become smaller when the ratio of the sheet thickness to the nugget diameter increases. Based on the approximate limit load solution, a general quadratic failure criterion for spot welds under combined three resultant forces and three resultant moments is proposed with correction factors determined by fitting to the experimental results of spot welds under combined loading conditions. The failure criterion can be used to characterize the failure loads of spot welds with consideration of the effects of sheet thickness, nugget diameter and combinations of loads. Experimental spot weld failure loads under combined opening and shear loading conditions and those under combined shear and twisting loading conditions are shown to be characterized well by the proposed failure criterion. Finally, a simplified general failure criterion for spot welds under three resultant forces and three resultant moments is proposed by neglecting the coupling terms of the resultant forces and moments for convenient use of the failure criterion for engineering applications.

Keywords: Resistance spot weld; Combined loading; Plastic limit analysis; Failure criterion

1. Introduction

Resistance spot welding is widely used to join sheet metals for automotive components. Accurate spot weld models are helpful in the structural integrity, durability, and crashworthiness analyses in the early automotive design stages. Since spot welds in automotive components are subjected to complex service

* Corresponding author. Tel.: +1-734-764-9404; fax: +1-734-647-3170.
E-mail address: jwo@umich.edu (J. Pan).

0020-7683/$ - see front matter © 2003 Elsevier Ltd. All rights reserved.
doi:10.1016/S0020-7683(03)00341-X

loading conditions, various types of specimens have been used to analyze fatigue lives of spot welds, for example, see Hartmann (1958), Davidson (1983), Radaj (1989), Wang and Ewing (1991), Swellam et al. (1994), Sheppard and Pan (2001) and Zhang (2001). The strengths of spot welds have also been investigated by many researchers. For example, Hartmann (1958) discussed the mechanical tests of spot welds in tension-shear, direct tension, torsion and peel specimens. VandenBossche (1977) adopted a plasticity approach to examine the strength of spot welds in lap-shear specimens. Sawhill and Furr (1981) and Ewing et al. (1982) investigated the strength of spot welds in terms of the specimen geometry, welding parameter, welding schedule, base metal strength, testing speed and testing configuration. Zuniga and Sheppard (1997) examined the failure modes of spot welds in coach-peel and lap-shear specimens. Lee et al. (1998) adopted a nominal stress approach to model their experimental results on the strength of spot welds in U shaped specimens under combined tension and shear loading conditions. Wung (2001a) and Wung et al. (2001) proposed a failure criterion based on their experimental results of spot welds in various types of specimens. Lin et al. (2001, 2002b) investigated the failure mechanisms of spot welds in mild and HSLA steel square-cup specimens by examining the fractographs of spot welds under combined opening and shear loading conditions. Lin et al. (2002a, 2003) obtained an approximate limit load solution for spot welds under combined opening and shear loading conditions and developed a failure criterion for spot welds in mild steel specimens under static and impact combined loading conditions based on their experimental results.

The experimental observations in Lin et al. (2001, 2002b) show that failure occurs along the circumference of the weld nuggets of spot welds in mild steel specimens. Fig. 1 shows the side views of failed 1.5 mm thickness specimens of mild steel under pure opening and combined opening and shear loading conditions. The arrows in the figure show the loading directions. Circumferential failure can be seen under pure opening loading conditions (with a loading angle of 0° as defined in Lin et al., 2001, 2002b) in Fig. 1(a). Circumferential failure with a remaining lip can also be seen under combined opening and shear loading conditions in Fig. 1(b). However, when the weld process is questionable or the weld has a weaker strength than the base metal, spot welds may have the interfacial failure mode (through nugget failure) as discussed in Thornton et al. (1996), Chao et al. (1998) and Peterson and Borchelt (2000).

Fig. 2 shows schematically two metal sheets jointed by a spot weld. Note that the spot weld is idealized as a circular cylinder as shown in Fig. 2. These two sheets could be different materials with different thicknesses. As schematically shown in Fig. 2(a), the surface tractions $\boldsymbol{T}_{\mathrm{u}}$ and $\boldsymbol{T}_{\mathrm{l}}$ are applied on the lateral sides of the upper and lower metal sheets, respectively. When the surface tractions increase, the spot welds may fail by different failure modes. Three possible different failure modes are shown in Fig. 2(b)–2(d) with shaded failure surfaces. Fig. 2(b) indicates that the failure of spot weld occurs along the circumferential surface of the spot weld in the lower sheet. Fig. 2(c) indicates that the failure of spot weld occurs along the circumferential surface of the spot weld in the upper sheet. Fig. 2(d) shows that the spot weld fails along the interfacial

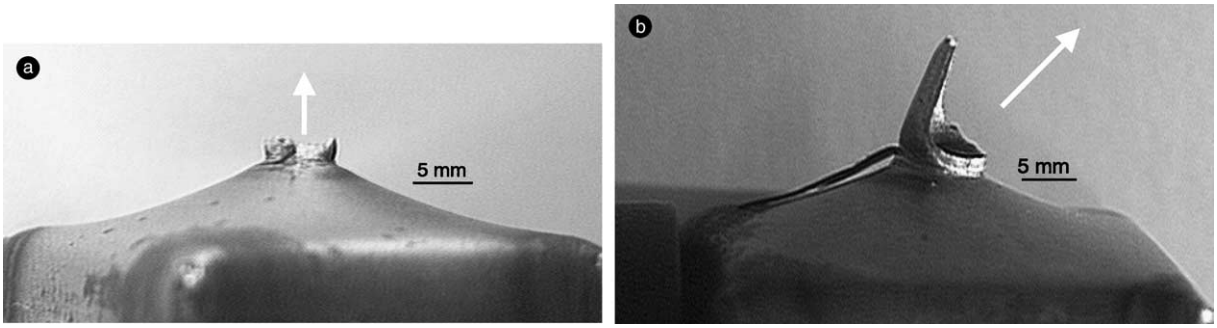

Fig. 1. Side views of 1.5 mm thickness specimens under (a) pure opening loading conditions and (b) combined opening and shear loading conditions. The arrows indicate the loading directions.

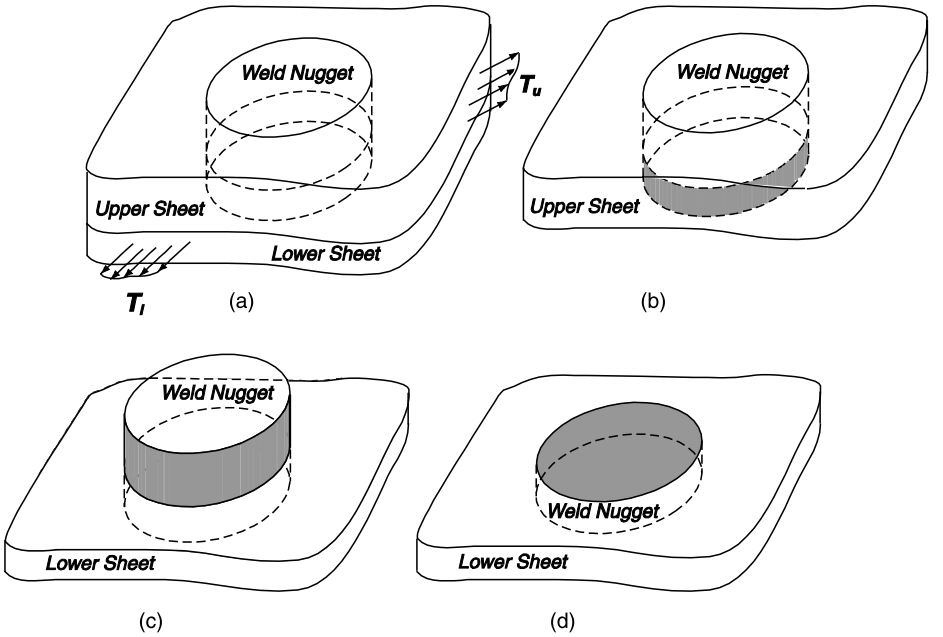

Fig. 2. Two sheets joined by a spot weld may fail under circumferential or interfacial failure modes. (a) Two sheet metals joined by a spot weld under surface tractions $\boldsymbol{T}_u$ and $\boldsymbol{T}_l$. (b) The spot weld may fail near the circumferential surface shown as the shaded region in the lower sheet. (c) The spot weld may fail near the circumferential surface shown as the shaded region in the upper sheet. (d) The spot weld may fail along the interfacial surface shown as the shaded region between the two sheets.

surface of the spot weld between two metal sheets. The failure of the spot weld is determined by the competition of these three failure modes (two circumferential failure modes and one interfacial failure mode). The spot weld fails when the load first satisfies one of the failure conditions of these three failure modes as the load increases. Therefore, the failure conditions need to be investigated for both circumferential and interfacial failure modes. In this paper, we will concentrate on the circumferential failure mode of spot welds.

Since spot welds in structural components often fail under combined loads during vehicle crashes, a general failure criterion for spot welds under combined loads is helpful for the crashworthiness analysis in the early automotive design stage. A general failure criterion for spot welds can be implemented into finite element codes for accurate simulations of the crush of spot welded structural components. In this paper, the failure mechanisms of spot welds under different loading conditions are first examined. We then try to investigate the failure loads of spot welds under combined three resultant forces and three resultant moments for the circumferential failure mode. An approximate limit load analysis is performed to investigate the effects of combinations of loads, sheet thickness and nugget diameter. Based on the approximate limit load solution and the experimental results, a general failure criterion is proposed. Finally, a simplified general failure criterion is proposed for easy use of the failure criterion for engineering applications.

2. Failure mechanisms

2.1. Experimental observations

A comparison of the micrographs shown in Lin et al. (2001, 2002b) suggests that extensive plastic deformation occurs near the circumferential surface when spot welds are subjected to loads to failure. The

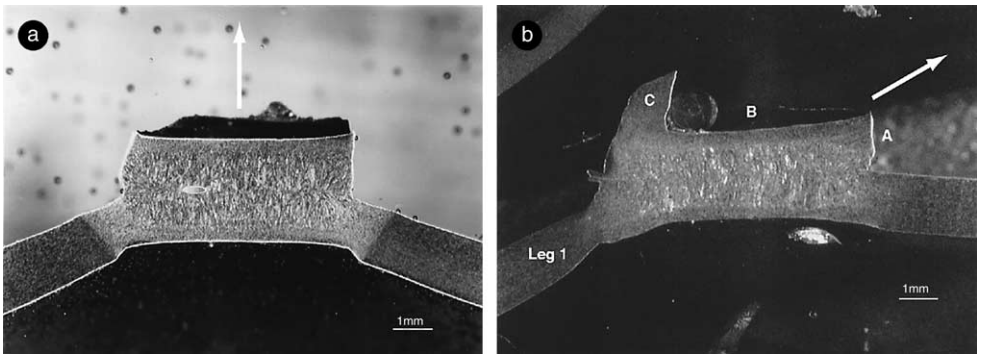

Fig. 3. (a) A micrograph of the cross-section of a failed spot weld in a 1.5 mm thickness specimen under pure opening loading conditions. (b) A micrograph of the cross-section of a failed spot weld in a 1.5 mm thickness specimen under combined opening and shear loading conditions.

failure mechanisms are asymmetrical when resultant shear forces were applied. Fig. 3(a) shows a micrograph of the cross-section of a failed spot weld in a 1.5 mm thickness specimen under opening loading conditions (Lin et al., 2002b). The arrow in the figure shows the loading direction. The figure shows that the spot weld appears to fail only by the through thickness shear near the nugget circumferential surface. Fig. 3(b) shows a micrograph of the cross-section of a failed spot weld in a 1.5 mm thickness specimen under combined opening and shear loading conditions (Lin et al., 2002b). Again, the arrow in the figure shows the loading direction. The load can be decomposed into an opening component to open the spot weld and a shear component to shear the spot weld. As shown in the figure, necking due to stretching appears close to the weld nugget in the left lower leg, as marked by Leg 1. Therefore, it appears that the fracture was initiated by necking/shear in the right upper leg at point A, as marked in Fig. 3(b). Then the failure propagated around the circumference of the nugget (marked by B) by necking/shear. Finally, the sheet metal on the top part of the specimen was torn off and left a lip (marked by C) on the spot weld after the two parts of the specimen separated. Based on observations from Figs. 1(b) and 3(b), spot welds failed initially near the right half nugget in the base metal when the resultant shear force induced more tensile stretching to the right half of the upper sheet near the nugget.

2.2. Plane stress finite element analysis

Lin et al. (2003) conducted a plane stress finite element analysis for a large square sheet with a circular rigid inclusion at the center to simulate a spot weld under shear loading conditions. In general, microhardness tests of steel spot welds show that the hardness is higher in the weld nugget than that of the base metal (for example, see Zuniga and Sheppard, 1995). The high hardness value in the weld nugget suggests a higher yield strength for the weld nugget than that of the base metal. When steel spot welds are subjected to large loads, large plastic deformation and failure occur outside the weld nugget as shown in Figs. 1 and 3. Therefore, the nugget is assumed to be a rigid circular inclusion in the plane stress finite element analysis in Lin et al. (2003). In Lin et al. (2003), the rigid circular inclusion is fixed and a positive displacement in the x direction is applied along the outer boundary of the sheet. The sheet material is assumed to follow an elastic perfectly plastic behavior. Fig. 4(a) shows an undeformed mesh of the finite element model near the rigid circular inclusion. Fig. 4(b) shows the contour of the plastic strain ε_{xx} from the finite element analysis based on the deformed mesh. Note that the displacement of the deformed mesh shown in the figure is magnified by 500% in order to show the deformation of elements clearly. As shown in Fig. 4(b), the tensile plastic strain ε_{xx} becomes large only near the right part of the circumferential surface. This suggests that the large

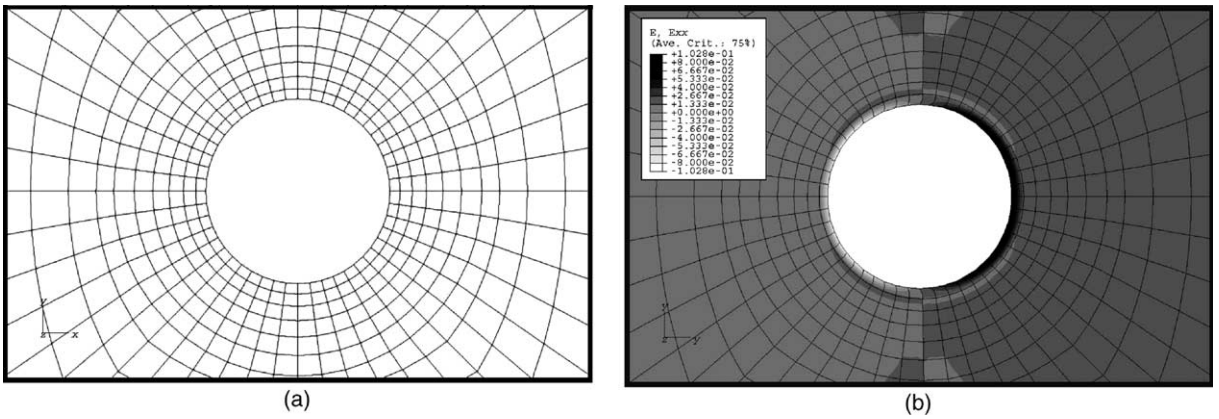

Fig. 4. (a) An undeformed mesh of the finite element model near the rigid circular inclusion. (b) Distribution of the plastic strain ε_{xx} near a rigid circular inclusion in a large thin sheet with in-plane displacement applied along the boundary.

tensile plastic strain ε_{xx} near the right part of the circumferential surface is most likely responsible for the necking/shear failure of the sheet metal for spot welds under shear dominant loading conditions. In summary, when spot welds are subjected to dominant in-plane shear loads, extensive tensile plastic deformation occurs only near a partial circumferential surface of the weld nugget. In order to develop a failure criterion for the spot welds under general combined loading conditions, plastic collapse is considered only on a partial nugget circumferential surface when resultant shear forces or moments are applied.

3. An approximate limit load analysis

Based on the experimental observations and finite element analysis, a limit load approach is adopted for spot welds under combined loading conditions. For the limit load approach, rigid perfectly plastic material behavior is first assumed. Note that the limit load approach is commonly used to obtain the maximum load carrying capacity of structures where plastic deformation is extensive at failure. For example, Merkle and Corten (1974) conducted a lower bound limit load analysis for the material ahead of the crack tip to estimate the J-integral for a compact tension specimen. In their lower bound limit load analysis, they mainly considered the global equilibrium. However, their approach still gave a good engineering solution which has been adopted in many subsequent engineering fracture analyses, for example, see Chapter 12 in Anderson (1995), and Pan (1984, 1986) for limit load analyses of cracked pipes. As for spot weld problems, the limit load approach conducted by Lin et al. (2002a) with consideration of the global equilibrium appears to give a good engineering solution to characterize the failure loads of spot welds under combined opening and shear loading conditions. We will follow the same strategy as the investigations mentioned earlier to develop an engineering solution under combined loading conditions.

Fig. 5(a) shows schematically two metal sheets joined by a spot weld. As shown in Fig. 5(a), the surface tractions $\boldsymbol{T}_{\mathrm{u}}$ and $\boldsymbol{T}_{\mathrm{l}}$ are applied on the lateral sides of the upper and lower metal sheets, respectively. As mentioned earlier, we idealize the weld nugget as a circular cylinder as shown in Fig. 5(a). Fig. 5(a) also shows a Cartesian coordinate system where x and y represent the in-plane coordinates, and z represents the out-of-plane coordinate. The origin of the Cartesian coordinate system is located at the center of the interfacial circular cross-section of the weld nugget between the two sheets as shown. Note that the directions of the x and y axes of the Cartesian coordinate system must coincide with the directions of the nominal principal bending moments of the sheet near the weld nugget to avoid the consideration of the twisting

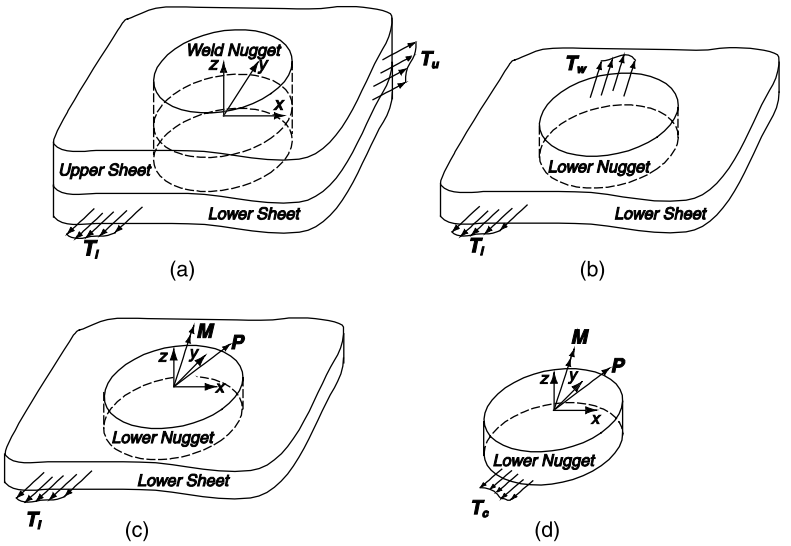

Fig. 5. (a) Two sheet metals are joined by a spot weld under the surface tractions $\boldsymbol{T}_u$ and $\boldsymbol{T}_l$. The surface tractions and a Cartesian coordinate system are shown. (b) The lower sheet with the lower half nugget is shown under the surface tractions $\boldsymbol{T}_l$ and $\boldsymbol{T}_w$. (c) The surface traction $\boldsymbol{T}_w$ on the top surface of the lower half nugget is represented by a resultant force $\boldsymbol{P}$ and a resultant moment $\boldsymbol{M}$. (d) The lower half nugget is considered solely with the surface traction $\boldsymbol{T}_c$ on the nugget circumferential surface to balance the resultant loads.

component of the nominal moments. For this limit load analysis, we only consider the lower half of weld nugget in the thinner sheet as shown in Fig. 5(b) without loss of generality. Fig. 5(b) shows that the surface traction $\boldsymbol{T}_w$ is on the top surface of the lower half nugget in the thinner sheet. Fig. 5(c) shows that the surface traction $\boldsymbol{T}_w$ can also be expressed as a resultant force $\boldsymbol{P}$ and a resultant moment $\boldsymbol{M}$ at the center of the interfacial nugget surface. If only the lower half nugget is considered, the resultant loads $\boldsymbol{P}$ and $\boldsymbol{M}$ should be balanced by the surface traction $\boldsymbol{T}_c$ along the nugget circumferential surface in a free body diagram for the lower half nugget as shown in Fig. 5(d).

Note that in order to develop a limit load solution, the equilibrium conditions need to be satisfied. In the main text, we only conducted an approximate limit load analysis with consideration of the global equilibrium conditions. The details and the difficulty to find a stress distribution to satisfy the local equilibrium conditions near the circumferential surface of the lower half nugget are discussed in Appendix A. Here, we consider the stresses along the nugget circumferential surface but with respect to the Cartesian coordinate system due to resultant loads $\boldsymbol{P}$ and $\boldsymbol{M}$. It is helpful to imagine that a rectangular box outside the lower half nugget as shown in Fig. 6(a) to evaluate the stresses along the nugget circumferential surface with respect to a Cartesian coordinate system. All the stresses with respect to Cartesian coordinate system along the circumferential surface of the lower half nugget are used to balance the resultant force and the resultant moment on the top surface of the lower half nugget. The resultant force and the resultant moment on the top surface of the lower half nugget are decomposed into three forces P_x, P_y and P_z and three moments M_x, M_y and M_z as shown in Fig. 6(a). The stresses with respect to the Cartesian coordinate system are expressed schematically in the physical directions to balance the positive resultant forces and resultant moments. Here, σ_{xx}, σ_{yy} and σ_{xy} represent the average in-plane stresses, and σ_{xz} and σ_{yz} represent the average out-of-plane shear stresses on the lateral surfaces. Note that, in this limit load analysis, we only consider the case of the lower half nugget under three forces, P_x, P_y and P_z, and two in-plane bending moments, M_x and M_y. The difficulty of considering the twisting moment M_z in this limit load analysis will be discussed in Appendix B. Note that a cylindrical coordinate system as shown in Fig. 6(b) is also adopted to conveniently to integrate

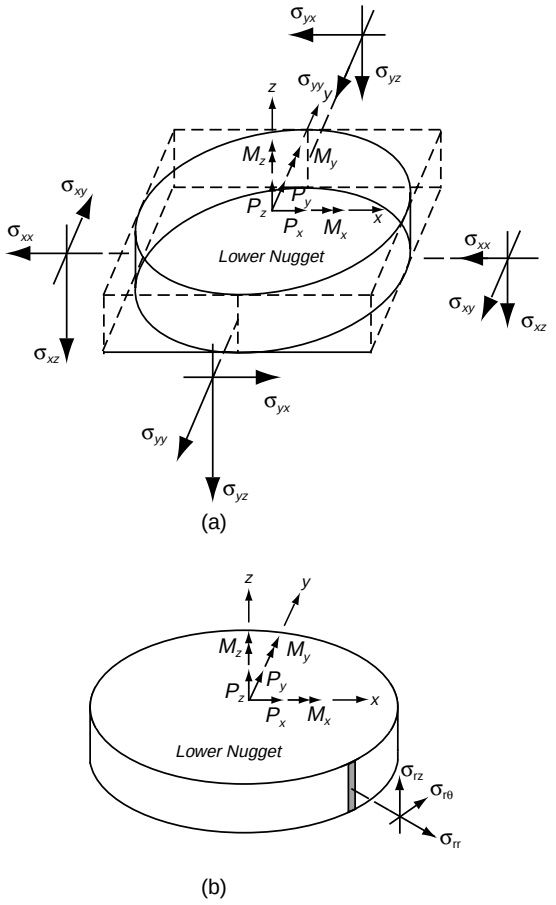

Fig. 6. The lower half nugget is subjected to the resultant force $\boldsymbol{P}$ and the resultant moment $\boldsymbol{M}$, which are decomposed into the components with respect to a Cartesian coordinate system. The resultant loads are balanced by the assumed stresses along the circumferential surface of the spot welds (a) in the Cartesian coordinate system and (b) in the cylindrical coordinate system.

the stresses along the circumferential surface to balance the resultant forces and moments on the top surface of the lower half nugget in the approximate limit load analysis. The von Mises yield criterion is employed to develop the approximate limit load solution. The detailed stress states on the circumferential surface of the weld nugget with respect to both the Cartesian and cylindrical coordinate systems due to each of the force and moment components are discussed in the following.

3.1. Stresses due to bending moments M_x and M_y

Fig. 7 shows a side view of the lower half nugget with assumed loads and average stresses. As shown in Fig. 7(a), an average shear stress $\sigma_{rz}^{M_y}$ acting on the circumferential surface of the nugget is assumed to balance the moment M_y. Here, $\sigma_{rz}^{M_y}$ represents the average value of σ_{rz} through the thickness due to the moment M_y. Note that the physical directions of $\sigma_{rz}^{M_y}$ due to M_y are shown in Fig. 7(a). Now, we are seeking a distribution of $\sigma_{rz}^{M_y}$ as a function of θ based on the assumption of the uniform shear stress $\sigma_{xz}^{M_y}$ along the

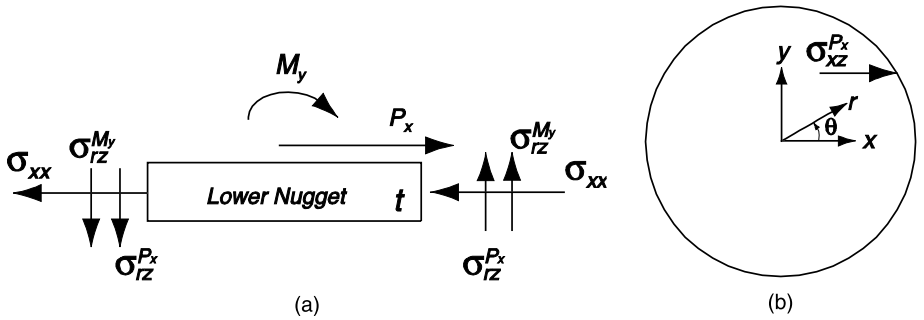

Fig. 7. (a) A side view of the lower half nugget under the moment M_y, the shear load P_x and the assumed stresses, (b) a top view of the shear stress $\sigma_{xz}^{P_x}$ due to the shear load P_x on the lower half nugget.

nugget circumference. Note that other contributions to the shear stress σ_{rz} due to the opening and shear loads will be discussed later. The shear stress $\sigma_{xz}^{M_y}$ can be referred to the cylindrical coordinate as

$$\sigma_{rz}^{M_y} = \sigma_{xz}^{M_y} \cos\theta \tag{1}$$

$$\sigma_{\theta z}^{M_y} = -\sigma_{xz}^{M_y} \sin\theta \tag{2}$$

Here, $\sigma_{rz}^{M_y}$ and $\sigma_{\theta z}^{M_y}$ represent the shear stress components due to the moment M_y. Since the moment M_y is balanced by the shear stress $\sigma_{rz}^{M_y}$, the moment balance in the y direction with respect to the lower half nugget requires

$$M_y - \int_0^{2\pi} \sigma_{rz}^{M_y} (r\cos\theta) t r \, \mathrm{d}\theta = 0 \tag{3}$$

where r is the nugget radius and t is the sheet thickness. Since $\sigma_{xz}^{M_y}$ is assumed to be a constant, $\sigma_{xz}^{M_y}$ can be derived as

$$\sigma_{xz}^{M_y} = \frac{M_y}{\pi r^2 t} = \frac{4M_y}{\pi D^2 t} \tag{4}$$

where D is the nugget diameter. Note that we need to use the cylindrical coordinate system to conveniently integrate the contribution of the shear stress $\sigma_{xz}^{M_y}$ to the bending moment. Similarly, we can obtain $\sigma_{yz}^{M_x}$ due to the moment M_x as

$$\sigma_{yz}^{M_x} = -\frac{M_x}{\pi r^2 t} = -\frac{4M_x}{\pi D^2 t} \tag{5}$$

3.2. Stresses due to shear loads P_x and P_y

3.2.1. Normal stresses

We assume that the shear loads P_x and P_y are balanced by the average normal stresses σ_{xx} and σ_{yy}. We now discuss the stress due to the shear load P_x first. Fig. 7(a) shows the side view of the weld nugget subjected to a shear load P_x and the corresponding stress σ_{xx}. The physical directions of σ_{xx} on the two sides of the nugget are shown in Fig. 7(a). The stress σ_{xx} due to shear load P_x is positive for the left part and negative for the right part of the lower half nugget as show in Fig. 7(a). One can consider that the assumed stress state comes from the fact that the shear load P_x on the surface of the lower half nugget pulls the left part of the adjacent material and pushes the right part of the adjacent material. The assumption of the

stress state is physical by referring to the deformed mesh as shown in Fig. 4(b). Note that the deformed mesh as shown in Fig. 4(b) can be related to the deformation mode of a spot weld under a negative resultant force P_x applied on the top surface of the lower half nugget. We here assume that the stresses σ_{rr}, $\sigma_{\theta\theta}$ and $\sigma_{r\theta}$ of the material element are derived from the stress state where σ_{xx} is uniform and $\sigma_{xy} = 0$ for the in-plane stresses for the left and right half of the nugget surface due to the shear load P_x. The average stress σ_{xx} through the thickness is assumed to act along the mid-plane of the lower half nugget. The normal stress σ_{xx} can be written as

$$\sigma_{xx} = \mp \frac{P_x}{2Dt} \tag{6}$$

In Eq. (6), "−" is for the right half of the lower nugget and "+" is for the left half of the lower nugget.

The stresses on the circumferential surface can now be referred to the cylindrical coordinate system as

$$\sigma_{rr}^{P_x} = \sigma_{xx} \cos^2 \theta \tag{7}$$

$$\sigma_{r\theta}^{P_x} = -\sigma_{xx} \sin\theta \cos\theta \tag{8}$$

$$\sigma_{\theta\theta}^{P_x} = \sigma_{xx} \sin^2 \theta \tag{9}$$

Similarly, the stress σ_{yy} due to the shear load P_y can be written as

$$\sigma_{yy} = \mp \frac{P_y}{2Dt} \tag{10}$$

Note that the stress σ_{yy} due to the shear load P_y is positive for the front part and negative for the back part of the lower half nugget as defined in Fig. 6(a). The stresses on the circumferential surface can also be referred to the cylindrical coordinate system as

$$\sigma_{rr}^{P_y} = \sigma_{yy} \sin^2 \theta \tag{11}$$

$$\sigma_{r\theta}^{P_y} = \sigma_{yy} \sin\theta \cos\theta \tag{12}$$

$$\sigma_{\theta\theta}^{P_y} = \sigma_{yy} \cos^2 \theta \tag{13}$$

Note that the sign of σ_{xx} is different for the right and the left part of the lower nugget and the sign of σ_{yy} is different for the front and back part of the lower nugget. Therefore, there are four stress states for σ_{xx} and σ_{yy} for the regions of $\theta = 0$ to $\pi/2$, $\pi/2$ to π, π to $3\pi/2$, and $3\pi/2$ to 2π along the circumferential surface.

3.2.2. Shear stresses

As shown in Fig. 7(a), an average shear stress $\sigma_{rz}^{P_x}$ acting on the circumferential surface of lower half nugget is needed to balance the moment due to the shear load P_x and the average stress σ_{xx}. Here, $\sigma_{rz}^{P_x}$ represents the average value of σ_{rz} through the thickness due to P_x. Now, we are seeking a distribution of $\sigma_{rz}^{P_x}$ as a function of θ. First, we consider a distribution of $\sigma_{xz}^{P_x}$ to represent the shear load P_x acting on the top surface of the lower half nugget as shown in Fig. 7(b). The shear stress due to P_x can be referred to the cylindrical coordinate system as

$$\sigma_{rz}^{P_x} = \sigma_{xz}^{P_x} \cos\theta \tag{14}$$

$$\sigma_{\theta z}^{P_x} = -\sigma_{xz}^{P_x} \sin\theta \tag{15}$$

Here, $\sigma_{rz}^{P_x}$ and $\sigma_{\theta z}^{P_x}$ represent the components of the shear stress due to the shear load P_x. Note that another contribution to the shear stress σ_{rz} due to the opening load P_z will be discussed later. The moment balance in the y direction with respect to the lower half nugget requires

$$\int_0^{2\pi} \sigma_{rz}^{P_x}(r\cos\theta)tr\,\mathrm{d}\theta - P_x \cdot \frac{t}{2} = 0 \tag{16}$$

When $\sigma_{xz}^{P_x}$ is assumed to be a constant, $\sigma_{xz}^{P_x}$ can be derived as

$$\sigma_{xz}^{P_x} = \frac{P_x}{2\pi r^2} = \frac{2P_x}{\pi D^2} \tag{17}$$

Similarly, the shear stress $\sigma_{yz}^{P_y}$ due to the shear load P_y can be written as

$$\sigma_{yz}^{P_y} = \frac{P_y}{2\pi r^2} = \frac{2P_y}{\pi D^2} \tag{18}$$

The shear stresses due to P_x and P_y can be referred to the cylindrical coordinate system as

$$\sigma_{rz} = \sigma_{xz}^{P_x}\cos\theta + \sigma_{yz}^{P_y}\sin\theta \tag{19}$$

$$\sigma_{\theta z} = -\sigma_{xz}^{P_x}\sin\theta + \sigma_{xz}^{P_y}\cos\theta \tag{20}$$

3.3. Stresses due to opening load P_z

Fig. 8(a) shows the lower half nugget under the opening load P_z on the interfacial surface and shear forces $P_{xz,\mathrm{right}}$, $P_{xz,\mathrm{left}}$, $P_{yz,\mathrm{back}}$ and $P_{yz,\mathrm{front}}$ on the circumference surface. The opening load P_z is balanced by shear forces $P_{xz,\mathrm{right}}$, $P_{xz,\mathrm{left}}$, $P_{yz,\mathrm{back}}$ and $P_{yz,\mathrm{front}}$. The equilibrium requires

$$P_z = P_{xz,\mathrm{right}} + P_{xz,\mathrm{left}} + P_{yz,\mathrm{back}} + P_{yz,\mathrm{front}} \tag{21}$$

Here, we define $P_{xz} = P_{xz,\mathrm{right}} + P_{xz,\mathrm{left}}$ and $P_{yz} = P_{yz,\mathrm{back}} + P_{yz,\mathrm{front}}$. Now, we define a distribution parameter α for spot welds under different opening loading conditions as

$$\alpha = \frac{P_{xz}}{P_z} \tag{22}$$

When we assume a spot weld as a spring with a point property in a finite element analysis, the transverse shear forces from the finite element analysis for the elements neighboring the spot welds can be obtained to determine α. For example, $\alpha = 1$ for spot welds under uniaxial opening loading conditions as in U shaped specimens used in Lee et al. (1998) and $\alpha = 0.5$ for spot welds under equal biaxial opening loading conditions as in square-cup specimens used in Lin et al. (2001). With the distribution parameter α, we can write

$$P_{xz} = \alpha P_z \tag{23}$$

and

$$P_{yz} = (1-\alpha)P_z \tag{24}$$

In order to account for more general opening loading conditions, we introduce two more distribution parameters as

$$\gamma_x = \frac{P_{xz,\mathrm{right}}}{P_{xz}} \tag{25a}$$

and

$$\gamma_y = \frac{P_{yz,\mathrm{back}}}{P_{yz}} \tag{25b}$$

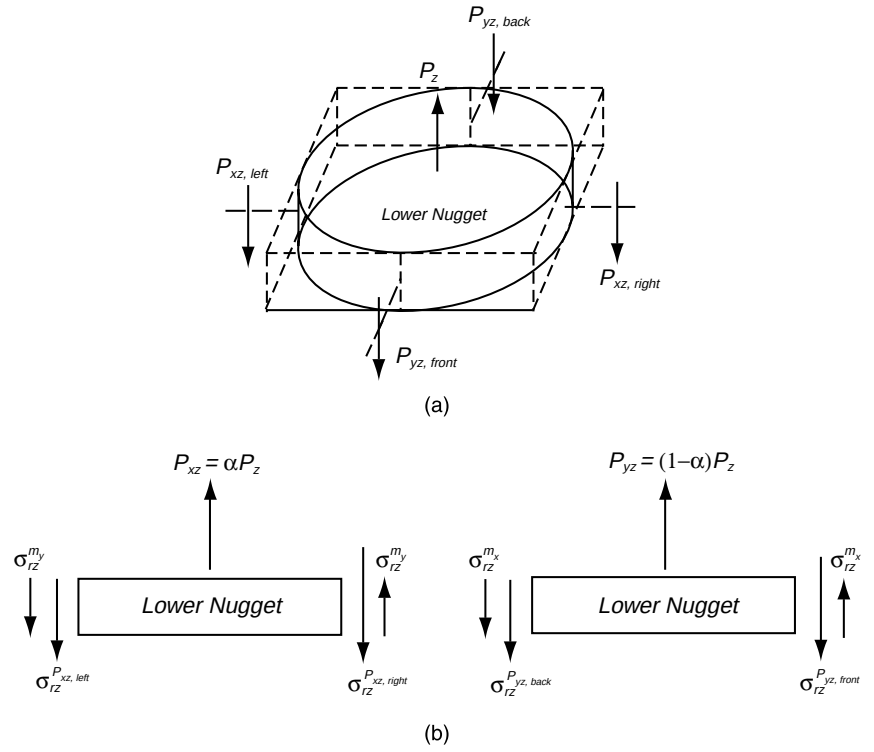

Fig. 8. (a) The lower half nugget subjected to the opening load P_z. The opening load P_z can be balanced by the shear forces $P_{xz,\mathrm{right}}$, $P_{xz,\mathrm{left}}$, $P_{yz,\mathrm{back}}$ and $P_{yz,\mathrm{front}}$ along the circumferential surface of the weld nugget. The imaginary box enclosed the spot weld is also shown for demonstration of selection of the shear forces. (b) The side views of the lower half nugget, viewed from the x axis and the y axis. The opening loads are balanced by the average shear stresses $\sigma_{rz}^{P_{xz,\mathrm{right}}}$, $\sigma_{rz}^{P_{xz,\mathrm{left}}}$, $\sigma_{rz}^{P_{yz,\mathrm{back}}}$ and $\sigma_{rz}^{P_{yz,\mathrm{front}}}$, due to the shear forces, $P_{xz,\mathrm{right}}$, $P_{xz,\mathrm{left}}$, $P_{yz,\mathrm{back}}$ and $P_{yz,\mathrm{front}}$, and the average shear stresses $\sigma_{rz}^{m_x}$ and $\sigma_{rz}^{m_y}$ due to unbalanced moments m_x and m_y.

Note that the two more distribution parameters are used to account for the different distributions of the shear forces P_{xz} and P_{yz} on the nugget circumferential surface. With the distribution parameters γ_x and γ_y, we can write

$$P_{xz,\mathrm{right}} = \gamma_x P_{xz} \tag{26}$$

$$P_{xz,\mathrm{left}} = (1-\gamma_x) P_{xz} \tag{27}$$

$$P_{yz,\mathrm{back}} = \gamma_y P_{yz} \tag{28}$$

$$P_{yz,\mathrm{front}} = (1-\gamma_y) P_{yz} \tag{29}$$

The values of distribution parameters γ_x and γ_y are between 0 and 1 based on the distributions of the opening load. For example, γ_x and γ_y are equal to 0.5 when the entire circumferential surface of the lower half nugget carries the load uniformly. If we assume that shear stresses $\sigma_{xz,\mathrm{right}}$, $\sigma_{xz,\mathrm{left}}$, $\sigma_{yz,\mathrm{back}}$ and $\sigma_{yz,\mathrm{front}}$, corresponding to $P_{xz,\mathrm{right}}$, $P_{xz,\mathrm{left}}$, $P_{yz,\mathrm{back}}$ and $P_{yz,\mathrm{front}}$, are uniformly distributed along the nugget circumferential surface. The average shear stresses $\sigma_{xz,\mathrm{right}}$, $\sigma_{xz,\mathrm{left}}$, $\sigma_{yz,\mathrm{back}}$ and $\sigma_{yz,\mathrm{front}}$ can be written as

$$\sigma_{xz}^{P_{xz,\mathrm{right}}} = -\frac{P_{xz,\mathrm{right}}}{Dt} = -\frac{\gamma_x P_{xz}}{Dt} = -\frac{\gamma_x \alpha P_z}{Dt} \tag{30}$$

$$\sigma_{xz}^{P_{xz,\text{left}}} = \frac{P_{xz,\text{left}}}{Dt} = \frac{(1-\gamma_x)P_{xz}}{Dt} = \frac{(1-\gamma_x)\alpha P_z}{Dt} \tag{31}$$

$$\sigma_{yz}^{P_{yz,\text{back}}} = -\frac{P_{yz,\text{back}}}{Dt} = -\frac{\gamma_y P_{yz}}{Dt} = -\frac{\gamma_y(1-\alpha)P_z}{Dt} \tag{32}$$

$$\sigma_{yz}^{P_{yz,\text{front}}} = \frac{P_{yz,\text{front}}}{Dt} = \frac{(1-\gamma_y)P_{yz}}{Dt} = \frac{(1-\gamma_y)(1-\alpha)P_z}{Dt} \tag{33}$$

Note that the stresses $\sigma_{xz}^{P_{xz,\text{right}}}$ and $\sigma_{yz}^{P_{yz,\text{back}}}$ are negative, and the stresses $\sigma_{xz}^{P_{xz,\text{left}}}$ and $\sigma_{yz}^{P_{yz,\text{front}}}$ are positive when a positive opening load P_z is applied on the lower half nugget. When the distribution parameters γ_x and γ_y are not equal to 0.5, shear stresses $\sigma_{xz}^{m_y}$ and $\sigma_{yz}^{m_x}$ along the circumferential surface are needed to balance the moments m_y and m_x, which are generated by the uneven shear forces $P_{xz,\text{right}}$, $P_{xz,\text{left}}$, $P_{yz,\text{back}}$ and $P_{yz,\text{front}}$. We now discuss the stresses due to the moment m_y first. As shown in Fig. 8(b), an average shear stress $\sigma_{rz}^{m_y}$ acting on the circumferential surface of the nugget is needed to balance the moment m_y generated by the shear forces $P_{xz,\text{right}}$ and $P_{xz,\text{left}}$. Here, $\sigma_{rz}^{m_y}$ represents the average value of σ_{rz} through the thickness due to m_y. As shown in Fig. 8(b), $\sigma_{rz}^{P_{xz,\text{right}}}$ and $\sigma_{rz}^{P_{xz,\text{left}}}$ represent the average values of σ_{rz} through thickness due to $P_{xz,\text{right}}$ and $P_{xz,\text{left}}$, respectively.

Now, we are seeking a distribution of σ_{rz}^{l} as a function of θ. Note that the superscript l of shear stress σ_{rz}^{l} represents the balancing moment m_y or uneven shear forces $P_{xz,\text{right}}$ and $P_{xz,\text{left}}$. The shear stress can be referred to the cylindrical coordinate system as

$$\sigma_{rz}^{l} = \sigma_{xz}^{l}\cos\theta \tag{34}$$

$$\sigma_{\theta z}^{l} = -\sigma_{xz}^{l}\sin\theta \tag{35}$$

Here, σ_{rz}^{l} and $\sigma_{\theta z}^{l}$ represent the components of the shear stress due to the balancing moment m_y or uneven shear forces $P_{xz,\text{right}}$ and $P_{xz,\text{left}}$. The equilibrium in the y direction requires

$$\int_{-\pi/2}^{\pi/2}\sigma_{rz}^{P_{xz,\text{right}}}(r\cos\theta)tr\,\mathrm{d}\theta + \int_{\pi/2}^{3\pi/2}\sigma_{rz}^{P_{xz,\text{left}}}(r\cos\theta)tr\,\mathrm{d}\theta + \int_{0}^{2\pi}\sigma_{rz}^{m_y}(r\cos\theta)tr\,\mathrm{d}\theta = 0 \tag{36}$$

When $\sigma_{xz}^{m_y}$ is assumed to be a constant, $\sigma_{xz}^{m_y}$ can be derived as

$$\sigma_{xz}^{m_y} = \frac{P_{xz}}{4rt}(2\gamma_x - 1) = \frac{\alpha P_z}{2Dt}(2\gamma_x - 1) \tag{37}$$

Similarly, we can obtain $\sigma_{yz}^{m_x}$ as

$$\sigma_{yz}^{m_x} = \frac{P_{yz}}{4rt}(2\gamma_y - 1) = \frac{(1-\alpha)P_z}{2Dt}(2\gamma_y - 1) \tag{38}$$

Based on the stress analyses, the total shear stresses σ_{xz} and σ_{yz} can be written as

$$\sigma_{xz} = \sigma_{xz}^{P_z} + \sigma_{xz}^{m_y} + \sigma_{xz}^{P_x} + \sigma_{xz}^{M_y} = \mp\frac{\alpha P_z}{2Dt} + \frac{2P_x}{\pi D^2} + \frac{4M_y}{\pi D^2 t} \tag{39}$$

$$\sigma_{yz} = \sigma_{yz}^{P_z} + \sigma_{yz}^{m_x} + \sigma_{yz}^{P_y} + \sigma_{yz}^{M_x} = \mp\frac{(1-\alpha)P_z}{2Dt} + \frac{2P_y}{\pi D^2} - \frac{4M_x}{\pi D^2 t} \tag{40}$$

In Eq. (39), "−" is for the right part and "+" is for the left part. In Eq. (40), "−" is for the back part and "+" is for the front part. Note that the stress σ_{xz} is different for the right and the left part of the nugget and the stress σ_{yz} is different for the front and back part of the nugget. Note that γ_x and γ_y do not appear in Eqs. (39) and (40), respectively. Therefore, there are four stress states for σ_{xz} and σ_{yz} for the regions of $\theta = 0$ to $\pi/2$, $\pi/2$ to π, π to $3\pi/2$, and $3\pi/2$ to 2π along the circumferential surface.

3.4. Approximate limit load solution

Based on the previous sections, the stress states in the Cartesian coordinate system along the circumferential surface of the nugget are obtained. Note that σ_{xx} and σ_{yy} are expressed in Eqs. (6) and (10), and σ_{xz} and σ_{yz} are expressed in Eqs. (39) and (40). As discussed earlier, the directions of the x and y axes of the Cartesian coordinate system are selected to coincide with those of the nominal principal bending moments of the sheet near the weld nugget to avoid the consideration of the twisting component of the nominal moments. Also, the twisting moment M_z is not considered in the approximate limit load analysis. Therefore, σ_{xy} is considered to be zero. Note that the difficulty of considering the twisting moment M_z in the approximate limit load analysis will be discussed in Appendix B. With the assumption of $\sigma_{zz} = 0$, the von Mises yield criterion can now be expressed as

$$\sigma_{xx}^2 - \sigma_{xx}\sigma_{yy} + \sigma_{yy}^2 + 3\sigma_{xz}^2 + 3\sigma_{yz}^2 = 3\tau_0^2 \tag{41}$$

where τ_0 is the shear yield stress.

Here, we define the effective shear stress τ_e as

$$\tau_e^2 = \frac{1}{3}\sigma_{xx}^2 - \frac{1}{3}\sigma_{xx}\sigma_{yy} + \frac{1}{3}\sigma_{yy}^2 + \sigma_{xz}^2 + \sigma_{yz}^2 \tag{42}$$

We can also define the normalized loads and moments as

$$\widetilde{P}_i = \frac{P_i}{2Dt\tau_0} \tag{43}$$

$$\widetilde{M}_j = \frac{M_j}{2Dt\tau_0}\frac{4}{\pi D} \tag{44}$$

where the subscript i represents x, y or z and the subscript j represents x and y. The normalized effective stress $\tilde{\tau}_e$ satisfying the yield criterion can be rewritten as

$$\tilde{\tau}_e^2 = \frac{1}{3}\widetilde{P}_x^2 + \frac{1}{3}\widetilde{P}_y^2 - \frac{1}{3}\mathrm{sign}(\sigma_{xx}^{P_x})\mathrm{sign}(\sigma_{yy}^{P_y})\widetilde{P}_x\widetilde{P}_y + \left[\mathrm{sign}(\sigma_{xz}^{P_z})\alpha\widetilde{P}_z + \widetilde{P}_x\left(\frac{4t}{\pi D}\right) + 2\widetilde{M}_y\right]^2 + \left[\mathrm{sign}(\sigma_{yz}^{P_z})(1-\alpha)\widetilde{P}_z + \widetilde{P}_y\left(\frac{4t}{\pi D}\right) - 2\widetilde{M}_x\right]^2 = 1 \tag{45}$$

Here, $\mathrm{sign}(\sigma_{xx}^{P_x})$, $\mathrm{sign}(\sigma_{yy}^{P_y})$, $\mathrm{sign}(\sigma_{xz}^{P_z})$ and $\mathrm{sign}(\sigma_{yz}^{P_z})$ represent the signs of corresponding stresses in each of the four regions. On the right hand side of Eq. (45), the first three terms related to σ_{xx} and σ_{yy} are due to P_x and P_y. The last two terms related to σ_{xz} and σ_{yz} are due to P_z, P_x, P_y, M_x and M_y. As shown in Fig. 9, we define region I for $\theta = 0$ to $\pi/2$, region II for $\theta = \pi/2$ to π, region III for $\theta = \pi$ to $3\pi/2$, and region IV for $\theta = 3\pi/2$ to 2π. The values of the four sign functions for the four regions are shown in Fig. 9. For a given monotonically increasing loading condition, when the stress state in one of regions satisfies the yield criterion ($\tilde{\tau}_e = 1$), the plastic collapse or failure is assumed to take place in the region. The details of plastic collapse condition are discussed in Appendix B. Note that, $\alpha = 1$ for uniaxial opening loading conditions and $\alpha = 1/2$ for equal biaxial opening loading conditions.

3.5. Special cases

Here we consider the case of combined opening load P_z and shear load P_x. Eq. (45) becomes

$$\tilde{\tau}_e^2 = \frac{1}{3}\widetilde{P}_x^2 + \left[\mathrm{sign}(\sigma_{xz}^{P_x})\alpha\widetilde{P}_z + \widetilde{P}_x\left(\frac{4t}{\pi D}\right)\right]^2 + [(1-\alpha)\widetilde{P}_z]^2 = 1 \tag{46}$$

For the case that both P_z and P_x are positive, the left half of the circumferential surface (regions II and III) with $\mathrm{sign}(\sigma_{xz}^{P_z}) = 1$ will first satisfy the yield criterion. Fig. 10 shows the approximate limit load solutions under

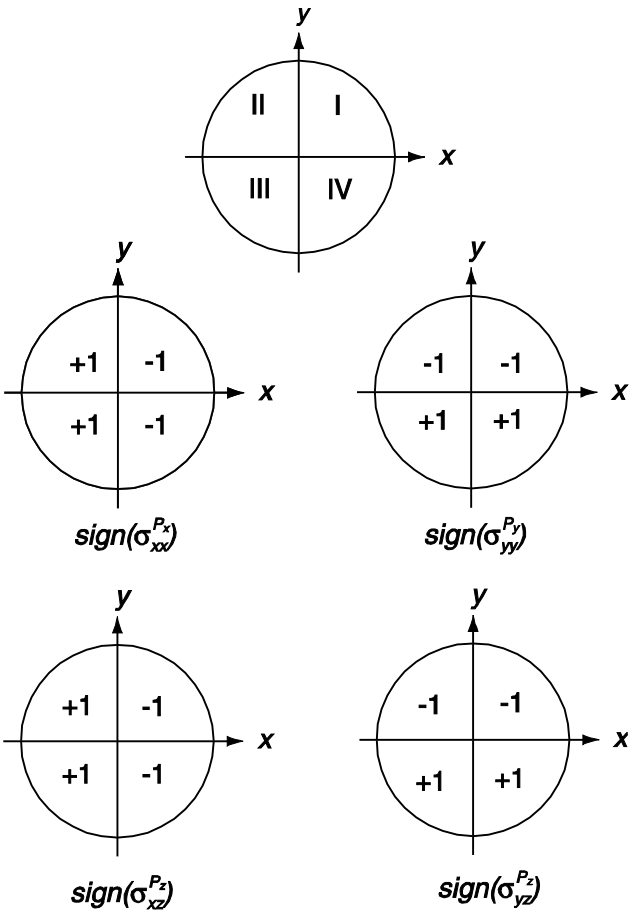

Fig. 9. The signs of the stresses in each of four regions in the yield criterion.

both equal biaxial ($\alpha = 0.5$) and uniaxial ($\alpha = 1$) opening loading conditions for spot welds with the ratios of $t/D = 0$, 0.1 and 0.2. Note that $t/D = 0$ represents the case that the thickness dependence is not presented in the yield criterion. As shown in Fig. 10, the normalized limit load $\overline{P}_z$ for spot welds under equal biaxial opening loading conditions is higher than that under uniaxial opening loading conditions for a given $\overline{P}_x$. Fig. 10 also shows that for a given $\overline{P}_x$, the normalized limit load $\overline{P}_z$ decreases when the ratio of t/D increases under both loading conditions. Note that, when we consider the case of pure opening modes ($\overline{P}_x = 0$), the ratio of the limit load under biaxial opening loading conditions to that under uniaxial opening loading conditions is $\sqrt{2}$ according to Eq. (46). This means that spot welds under biaxial opening loading conditions can carry 41% more loads than those under uniaxial opening loading conditions as shown in Fig. 10.

4. A general failure criterion

In order to develop a general failure criterion for spot welds under combined loading conditions, the limit loads in the yield criterion of Eq. (45) are modified to fit the experimental failure loads under combined loading conditions. First, the failure loads from combined load experiments are normalized as

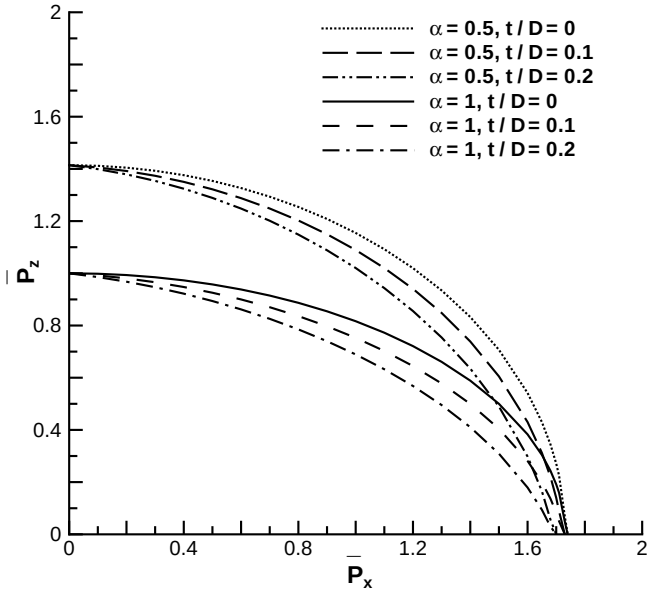

Fig. 10. The yield contours in terms of $\overline{P}_z$ and $\overline{P}_x$ for spot welds under combined loading conditions with various ratios of t/D. Here, both biaxial and uniaxial opening loads with $\alpha = 0.5$ and 1, respectively, are considered.

$$\overline{P}_i = \frac{P_i}{P_{\max}} \tag{47}$$

$$\overline{M}_i = \frac{M_i}{P_{\max}} \frac{4}{\pi D} \tag{48}$$

where the subscript i represents x, y or z and $P_{\max}$ represents the failure load of spot welds under pure uniaxial opening loading conditions. Based on the experimental results and the approximate limit load solution in Eq. (45), a general failure criterion is proposed as

$$\frac{1}{3}(k_{P_{xy}}\overline{P}_x)^2 + \frac{1}{3}(k_{P_{xy}}\overline{P}_y)^2 - \frac{1}{3}\mathrm{sign}(\sigma_{xx}^{P_x})\mathrm{sign}(\sigma_{yy}^{P_y})k_{P_{xy}}^2\overline{P}_x\overline{P}_y + (k_{M_z}\overline{M}_z)^2 + \left[\mathrm{sign}(\sigma_{xz}^{P_z})\alpha\overline{P}_z + k_{P_{xy}}\overline{P}_x\left(\frac{4t}{\pi D}\right) + 2k_{M_{xy}}\overline{M}_y\right]^2 + \left[\mathrm{sign}(\sigma_{yz}^{P_z})(1-\alpha)\overline{P}_z + k_{P_{xy}}\overline{P}_y\left(\frac{4t}{\pi D}\right) - 2k_{M_{xy}}\overline{M}_x\right]^2 = 1 \tag{49}$$

Here, the contribution of the twisting moment is accounted for by assuming a quadratic term of $\overline{M}_z^2$ to fit the experimental results. In Eq. (49), we include only three correction factors, $k_{P_{xy}}$, k_{M_z} and $k_{M_{xy}}$, to fit the experimental results based on the assumption of material in-plane isotropy within the x–y plane.

In order to demonstrate the applicability of the general failure criterion for mild steel spot welds, we first consider the case of spot welds under combined opening and shear loads. For the case that both P_x and P_z are positive, the left half of the circumferential surface (regions II and III) with $\mathrm{sign}(\sigma_{xz}^{P_z}) = 1$ will first satisfy the yield condition. For this case, Eq. (49) is reduced to

$$\frac{1}{3}(k_{P_{xy}}\overline{P}_x)^2 + \left[\alpha\overline{P}_z + k_{P_{xy}}\overline{P}_x\left(\frac{4t}{\pi D}\right)\right]^2 + [(1-\alpha)\overline{P}_z]^2 = 1 \tag{50}$$

Based on the experimental results for U shaped specimens ($\alpha = 1$) presented in Lee et al. (1998) and those for square-cup specimens ($\alpha = 0.5$) presented in Lin et al. (2002a), $k_{P_{xy}}$ can be estimated as 1.11 for these mild steel specimens. Fig. 11 shows the results based on the failure criterion in Eq. (50) and the results of

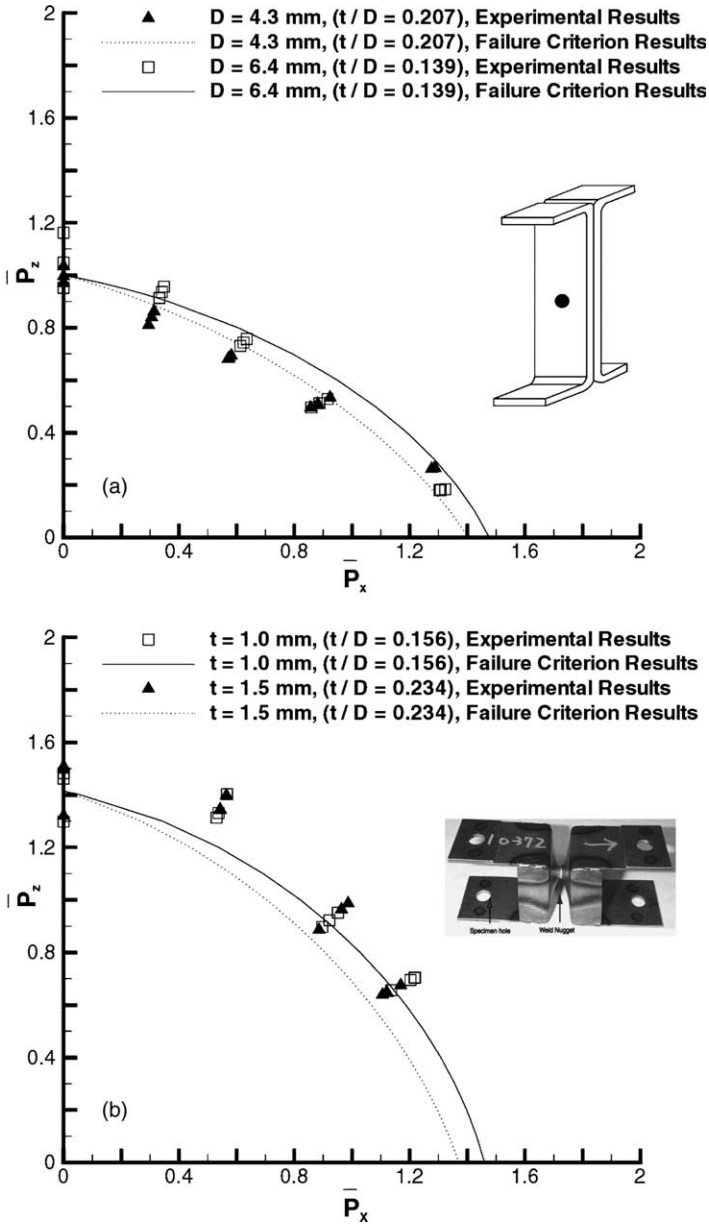

Fig. 11. (a) The normalized failure loads for spot weld with two different nugget sizes in U shaped specimens under combined opening and shear loads. Various symbols represent the experimental results and two different lines represent the results based on the failure criterion in Eq. (50). (b) The normalized failure loads for spot welds in square-cup specimens with two different thicknesses under combined opening and shear loads. Various symbols represent the experimental results and two different lines represent the results based on the failure criterion in Eq. (50).

experiments for spot welds under combined opening and shear loading conditions. Fig. 11(a) shows the normalized failure loads as various symbols for mild steel spot welds in U shaped specimens under combined opening and shear loads (Lee et al., 1998). A picture of the U shaped specimen is also shown as an insert in the figure. These experimental data were obtained from two different nugget diameters ($D = 4.3$ and 6.4 mm) and one sheet thickness ($t = 0.89$ mm). Note that the U shaped specimens are subjected to uniaxial opening loading conditions and therefore $\alpha = 1$. The experimental results are normalized by the maximum load of U shaped specimens under pure opening loading conditions. In the figure, the solid and dotted lines represent the results based on the failure criterion in Eq. (50). The failure contours appear to agree well with the experimental results. As shown in Fig. 11(a), when the ratio t/D increases, the failure contours based on both the experiments and the failure criterion in Eq. (50) become smaller.

Fig. 11(b) shows the normalized failure loads as various symbols for mild steel spot welds in square-cup specimens under combined opening and shear loads (Lin et al., 2002a). A picture of the square-cup specimen is also shown as an insert in the figure. These experimental data were obtained from one nugget diameter ($D = 6.4$ mm) and two different sheet thicknesses ($t = 1$ and 1.5 mm). Note that the specimens are subjected to equal biaxial opening loading conditions and therefore $\alpha = 0.5$. The experimental results should be normalized by the maximum load of U shaped specimens under pure uniaxial opening loading conditions. However, the maximum load for U shaped specimens for this mild steel is not available. The maximum load for U shaped specimens is therefore estimated from the maximum loads for the cup specimens divided by $\sqrt{2}$. In the figure, the solid and dotted lines represent the results based on the failure criterion in Eq. (50). The failure contours appear to agree with the experimental results with slight underestimation. As shown in Fig. 11(b), when the ratio t/D increases, the failure contours based on both the experiments and the failure criterion in Eq. (50) become smaller. As shown in Fig. 10(a) and 10(b), the normalized limit load $\overline{P}_z$ shown in Fig. 11(a) is lower for spot welds in U shaped specimens under uniaxial opening loading conditions than that in square-cup specimens shown in Fig. 11(b) under equal biaxial opening loading conditions for a given $\overline{P}_x$. The results based on the experiments and the failure criterion in Eq. (50) shown in Fig. 10(a) and 10(b) demonstrate the need of α in the failure criterion in Eq. (50).

Finally, we examine the case of spot welds under combined twisting moment M_z, and shear load P_x. Eq. (49) is reduced to

$$\left[\frac{1}{3}+\left(\frac{4t}{\pi D}\right)^2\right](k_{P_{xy}}\overline{P}_x)^2+(k_{M_z}\overline{M}_z)^2=1 \tag{51}$$

Note that the effect of bending due to the shear load P_x is accounted for by the term containing $4t/\pi D$ in Eq. (51). The factor $k_{P_{xy}}$ is estimated to be 1.11 based on the experimental results under combined opening and shear loading conditions. By comparing the experimental results, the effect of the twisting moment M_z is accounted for by a quadratic term of $(k_{M_z}M_z)^2$ in Eq. (51). Experimental results under combined twisting and shear loading conditions are available from Wung (2001b) using asymmetric lap-shear specimens where the weld nuggets are not located along the load application lines or the symmetric lines of the specimens. Fig. 12 shows the normalized experimental results as symbols and the results based on the failure criterion in Eq. (51) as a solid line for mild steel spot welds under combined twisting and shear loading conditions (Wung, 2001b). A picture of the asymmetric lap-shear specimen is also shown as an insert in the figure. These experimental data were obtained from one nugget diameter ($D = 6.7$ mm) and one sheet thickness ($t = 0.91$ mm). The failure contour appears to agree well with the experimental results. Note that the twisting moment M_z and the shear load P_x are normalized by the maximum load under pure uniaxial opening loading conditions. The maximum load under pure uniaxial opening loading conditions is estimated by Eq. (51) and the experimental maximum load for symmetric or regular lap-shear specimens where the twisting moment M_z is zero at the nugget. According to the normalized experimental results shown in Fig. 12, the factor k_{M_z} can be estimated as 1.08. When the testing results for spot welds in other types of

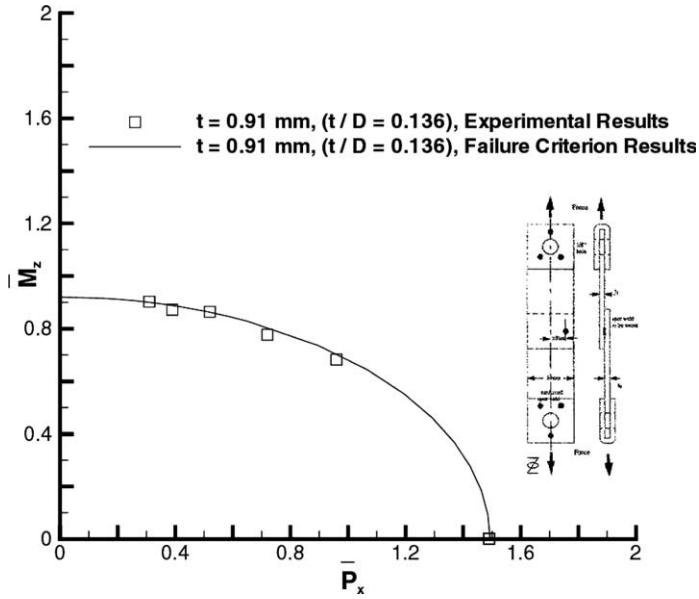

Fig. 12. The normalized failure loads for specimens under combined twisting and shear loading conditions. The symbols represent the experimental results and the solid line represents the results based on the failure criterion in Eq. (51).

specimens are available, we can determine the third correction factor $k_{M_{xy}}$. The correction factors in general depend upon the weld nugget size, sheet thickness, sheet material and welding process.

5. A simplified general failure criterion for spot welds

The failure loads of spot welds under combined loading conditions can be obtained by the general failure criterion based on Eq. (49). However, before we adopt this failure criterion, we need to determine the directions of the principal bending moments for the base metal sheet near the spot weld of interest. Note that our Cartesian coordinate system should be fixed to the directions of the principal bending moments to avoid the consideration of the moment M_{xy}. When the load distribution near the spot weld becomes complex, the distribution parameter α needs to be estimated. However, this procedure may not be convenient for implementation of the general failure criterion into finite element codes since the components or vehicles needed to be analyzed may contain hundreds or thousands of spot welds. In order to develop a failure criterion for spot welds for easy use, we propose a simplified general failure criterion for spot welds by neglecting the coupling terms of the resultant forces and moments as

$$[1-2\alpha+2\alpha^2]\overline{P}_z^2+k_{P_{xy}}^2\left[\frac{1}{3}+\left(\frac{4t}{\pi D}\right)^2\right](\overline{P}_x^2+\overline{P}_y^2)+k_{M_z}^2\overline{M}_z^2+4k_{M_{xy}}^2(\overline{M}_x^2+\overline{M}_y^2)=1 \tag{52}$$

where α depends upon the local transverse shear force ratio as in Eqs. (23) and (24) near the spot weld. Note again the forces and moments are still normalized by the pure uniaxial opening failure loads. On the left hand side of Eq. (52), the first term represents the contribution from the out-of-plane opening force, the second term represents the contribution from in-plane shear force, the third term represents the contribution from the twisting moment with respect to the out-of-plane coordinate z, and the fourth term rep-

resents the contribution from the in-plane bending moment. These three correction factors $k_{P_{xy}}$, k_{M_z} and $k_{M_{xy}}$ are determined from the experimental results under combined loading conditions.

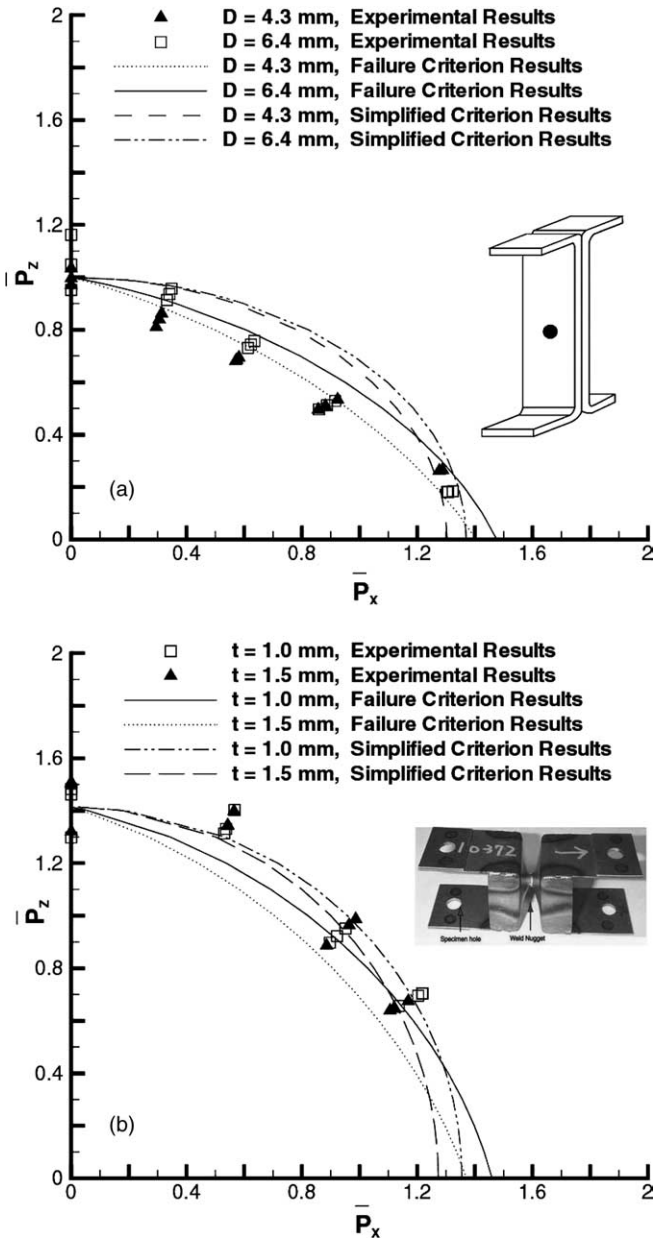

Fig. 13. (a) The normalized failure loads for spot weld with two different nugget sizes in U shaped specimens under combined opening and shear loads. Various symbols represent the experimental results and different lines represent the results based on the failure criterion in Eq. (50) and the simplified failure criterion in Eq. (53). (b) The normalized failure loads for spot welds in square-cup specimens with two different thicknesses under combined opening and shear loads. Various symbols represent the experimental results and different lines represent the results based on the failure criterion in Eq. (50) and the simplified failure criterion in Eq. (53).

In order to understand the difference between the simplified general failure criterion in Eq. (52) and the failure criterion in Eq. (49), the experimental results for spot welds under combined opening and shear loading conditions are used to compare the results based on the both failure criteria. For this loading condition, Eq. (52) is reduced to

$$[1-2\alpha+2\alpha^2]\overline{P}_z^2+\left[\frac{1}{3}+\left(\frac{4t}{\pi D}\right)^2\right](k_{P_{xy}}\overline{P}_x)^2=1 \tag{53}$$

Based on the experimental results for U shaped specimens ($\alpha=1$) presented in Lee et al. (1998) and those for square-cup specimens ($\alpha=0.5$) in Lin et al. (2002a), $k_{P_{xy}}$ can now be estimated as 1.25. Fig. 13 shows the results based on the failure criterion in Eq. (50) and the simplified failure criterion in Eq. (53), and the experimental results under combined opening and shear loading conditions. Fig. 13(a) shows the normalized failure loads as various symbols for mild steel spot welds in U shaped specimens under combined opening and shear loads (Lee et al., 1998). A picture of the U shaped specimen is also shown as an insert in the figure. Note that the U shaped specimens are subjected to uniaxial opening loading conditions and therefore $\alpha=1$. In the figure, the solid and dotted lines represent the results based on the failure criterion in Eq. (50) and the dashed-doted and dashed lines represent the results based on the simplified failure criterion in Eq. (53). The failure contours based on the failure criterion in Eq. (50) appear to agree with the experimental results. The failure contours based on the simplified failure criterion in Eq. (53) are slightly larger than those based on the failure criterion in Eq. (50) under combined opening and shear loading conditions. Fig. 13(b) shows the normalized failure loads as various symbols for mild steel spot welds in square-cup specimens under combined opening and shear loads (Lin et al., 2002a). A picture of the square-cup specimen is also shown as an insert in the figure. Note that the specimens are subjected to equal biaxial opening loading conditions and therefore $\alpha=0.5$. In the figure, the solid and dotted lines represent the results based on the failure criterion in Eq. (50) and the dashed-doted and dashed lines represent the results based on the simplified failure criterion in Eq. (53). As shown in Fig. 13(b), the failure contours based on the simplified failure criterion appear to agree better with the experimental results than those based on the failure criterion in Eq. (50) under combined opening and shear loading conditions.

6. Conclusions

Failure loads of spot welds under combined three resultant forces and three resultant moments are investigated. In order to obtain a general failure criterion for spot welds in circumferential failure mode for automotive applications, an approximate limit load analysis is performed. An approximate limit load solution is obtained with consideration of the effects of sheet thickness, nugget diameter and combination of loads. Based on the approximate limit load solution, a general failure criterion in a quadratic form for spot welds under combined loading conditions is proposed in terms of the normalized forces and moments with consideration of the sheet thickness and the nugget diameter. The general failure criterion includes three correction factors which can be estimated based on the experimental results of spot welds under combined loading conditions. The experimental results of failure loads under various combined loading conditions are compared well with those based on the general failure criterion with these correction factors. For convenient use of the failure criterion for engineering applications, a simplified general failure criterion is proposed under combined loading conditions. The results based on the simplified general failure criterion agree with the experimental results for specimens under combined opening and shear loading conditions. It appears that the simplified general failure criterion can be a good candidate for further research on determination of spot weld failure under arbitrary combined loading conditions by finite element computations.

Acknowledgements

The support of this work by Ford University Research Program is greatly appreciated. Helpful discussions with Dr. S.C. Tang of the University of Michigan are also greatly appreciated. Finally, the authors appreciate the comments from an anonymous reviewer. These comments lead to the final version of the paper.

Appendix A. Local equilibrium for limit load analysis

Fig. 14 shows schematically a two-strip model for the lower half nugget for the limit load analysis. A Cartesian coordinate system is also shown. The origin of the Cartesian coordinate system is located at the center of the top circular surface of the lower half nugget. The resultant loads $\boldsymbol{P}$ and $\boldsymbol{M}$ are applied on the top surface of the lower half nugget as shown. As shown in Fig. 14, strips A and B are parallel to the in-plane coordinates x and y, respectively. The width of strips A and B equals to the nugget diameter. The boundary of the strips represents the stress discontinuity lines. Note that the concept of stress discontinuity lines is widely used in the lower bound limit load analysis of cracked specimens under bending conditions. In this two-strip model, the lower half nugget is considered as a rigid circular cylinder. The stress $\sigma_{xx}^{P_x}$ is uniformly distributed in the right and left parts of strip A with the rigid lower half nugget excluded. The stress $\sigma_{yy}^{P_y}$ is uniformly distributed in the front and back parts of strip B with the rigid lower half nugget excluded. As shown in Fig. 14, the two strips and the weld nugget intersect with each other and provide four independent regions bordered by the nugget circumferential surface and the outer surface of the square box marked as bold lines as shown. Note that there is no connection between any two neighboring regions. Therefore, there is no requirement of the stress continuity between any two neighboring regions. When the stresses σ_{xz} and σ_{yz} due to each resultant are considered, it becomes difficult to obtain a stress distribution to satisfy the local equilibrium conditions throughout the domain of the two strips of the two-strip model. We will discuss this difficulty by examining the local equilibrium conditions.

The local equilibrium conditions with respect to the Cartesian coordinate system can be written as

$$\frac{\partial \sigma_{xx}}{\partial x}+\frac{\partial \sigma_{yx}}{\partial y}+\frac{\partial \sigma_{zx}}{\partial z}=0 \tag{A.1}$$

$$\frac{\partial \sigma_{xy}}{\partial x}+\frac{\partial \sigma_{yy}}{\partial y}+\frac{\partial \sigma_{zy}}{\partial z}=0 \tag{A.2}$$

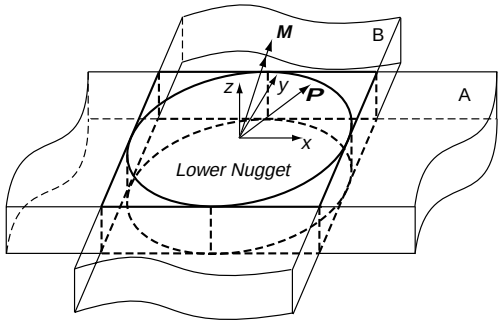

Fig. 14. A two-strip model of the lower half spot weld nugget for the limit load analysis.

$$\frac{\partial \sigma_{xz}}{\partial x}+\frac{\partial \sigma_{yz}}{\partial y}+\frac{\partial \sigma_{zz}}{\partial z}=0 \tag{A.3}$$

Here, the stresses in Eqs. (A.1)–(A.3) are average stresses through the thickness. Now we consider the sheet outside the nugget, the out-of-plane stresses σ_{zz}, σ_{zx} and σ_{zy} should vanish on the sheet surfaces. However, σ_{zx} and σ_{zy} are still considered as the average out-of-plane shear stresses through the thickness. Note that σ_{xy} is assumed to be zero since the twisting moment M_z is not considered in this limit load analysis. The equilibrium equations are now rewritten as

$$\frac{\partial \sigma_{xx}}{\partial x}=0 \tag{A.4}$$

$$\frac{\partial \sigma_{yy}}{\partial y}=0 \tag{A.5}$$

$$\frac{\partial \sigma_{xz}}{\partial x}+\frac{\partial \sigma_{yz}}{\partial y}=0 \tag{A.6}$$

We will consider the stresses due to the five resultant forces and moments, P_x, P_y, P_z, M_x and M_y, one by one. Denote the stresses with a subscript i as the stresses satisfy the equilibrium equations due to the ith resultant. Therefore, we can write the equilibrium equations for the stresses due to the ith resultant as

$$\frac{\partial (\sigma_{xx})_i}{\partial x}=0 \tag{A.7}$$

$$\frac{\partial (\sigma_{yy})_i}{\partial y}=0 \tag{A.8}$$

$$\frac{\partial (\sigma_{xz})_i}{\partial x}+\frac{\partial (\sigma_{yz})_i}{\partial y}=0 \tag{A.9}$$

Taking the summation of Eqs. (A.7)–(A.9) over the range of i from 1 to 5 gives

$$\frac{\partial \left(\sum_i \sigma_{xx}\right)_i}{\partial x}=0 \tag{A.10}$$

$$\frac{\partial \left(\sum_i \sigma_{yy}\right)_i}{\partial y}=0 \tag{A.11}$$

$$\frac{\partial \left(\sum_i \sigma_{xz}\right)_i}{\partial x}+\frac{\partial \left(\sum_i \sigma_{yz}\right)_i}{\partial y}=0 \tag{A.12}$$

Eqs. (A.10)–(A.12) indicate that when the stresses due to each resultant can be shown to satisfy the equilibrium equations, the sums of the stresses due to all the resultants should also satisfy the equilibrium equations.

As discussed in the main text, the stresses $\sigma_{xx}^{P_x}$ and $\sigma_{yy}^{P_y}$ due to P_x and P_y, respectively, are assumed to be uniformly distributed in the two-strip model as shown in Fig. 14. Since these stresses are uniformly distributed, equilibrium Eqs. (A.7) and (A.8) are satisfied. The statement is true when either the Cartesian or cylindrical coordinate system is used. When the stresses $\sigma_{xz}^{M_y}$, $\sigma_{xz}^{P_x}$, $\sigma_{xz}^{P_z}$ due to M_y, P_x, and P_z, and the stresses $\sigma_{yz}^{M_x}$, $\sigma_{yz}^{P_y}$, $\sigma_{yz}^{P_z}$ due to M_x, P_y and P_z are considered, we may select $(\sigma_{xz})_i$ independent of x and $(\sigma_{yz})_i$ independent of y to satisfy the average out-of-plane stress equilibrium condition in Eq. (A.9). However, it is difficult to obtain a stress distribution as a function of the in-plane coordinates x and y, and the thickness

coordinate z to satisfy the local average stress equilibrium condition in Eq. (A.9) and the moment equilibrium conditions in the x and y directions throughout the domain of the two strips of the two-strip model. Note that we neglect the flexural effects since we only concentrate on the material element bordering the nugget circumferential surface due to the observed failure mechanisms in Figs. 1 and 3. However, in order to satisfy the local average stress equilibrium condition in Eq. (A.9) and the moment equilibrium conditions, a much more complex stress state with the bending stress must be assumed for the material element away from the circumferential surface. With the consideration of the bending stress, the normal stresses such as σ_{xx} and σ_{yy} can no longer be assumed uniformly distributed through the thickness. This leads to a plastic collapse conditions on a part of the thickness. Moreover, if we consider the flexural effects away from the nugget circumferential surface, we should also consider the flexural effects for the material element bordering the nugget circumferential surface. The distribution of the local moment along the circumferential surface can be quite complex even under a relatively simple loading condition such as the pure opening loading condition. But this will also lead to a collapse condition on a part of the thickness. It seems that to develop a relative simple average stress and moment distribution to satisfy the local equilibrium conditions including flexural effects is a formidable task. Therefore, we relax the local equilibrium conditions and concentrate on the material element bordering the nugget circumferential surface to satisfy the global equilibrium conditions in order to obtain an approximate closed form engineering solution in the same spirit of the analysis of Merkle and Corten (1974). In this way, the engineering solution will provide a basic form for the failure criterion in terms of appropriately normalized resultants.

In this paper, we only consider the four thin layers bordering the lower half nugget in the four independent regions as shown in Fig. 15. Note that Fig. 15 shows a top view of the two-strip model. The shaded areas represent four independent regions. Dashed lines as shown in the figure represent four thin material layers bordering the rigid lower half nugget. The approximate limit load analysis is conducted for these four independent thin layers. Strictly speaking, the lower bound limit load analysis should be conducted with statically admissible stresses in a finite domain instead of a thin layer with the equilibrium and traction continuity conditions being satisfied. However, in order to develop a closed form engineering failure criterion of spot welds for easy use, it is only feasible to conduct the approximate limit load analysis for the four thin material layers bordering the weld nugget due to the complex stress state experienced by spot welds under combined resultant force and moment conditions.

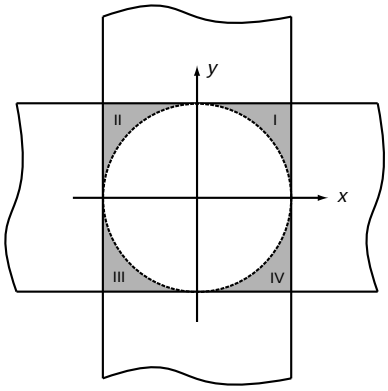

Fig. 15. A top view of the two-strip model for the lower half spot weld nugget. Four independent regions are marked as four shaded areas. Dashed lines are shown in the figure to represent actually failure locations in each region.

Appendix B. Stresses due to twisting moment M_z and plastic collapse conditions

Here, the difficulty of considering the twisting moment M_z in the approximate limit load analysis is discussed. We assume that the twisting moment M_z is balanced by the shear stress $\sigma_{r\theta}^{M_z}$ with respect to the cylindrical coordinate system. Considering the global equilibrium conditions, $\sigma_{r\theta}^{M_z}$ is written as

$$\sigma_{r\theta}^{M_z} = -\frac{M_z}{2\pi r^2 t} = -\frac{2M_z}{\pi D^2 t} \tag{B.1}$$

The other two in-plane stresses $\sigma_{rr}^{M_z}$ and $\sigma_{\theta\theta}^{M_z}$ are assume as

$$\sigma_{\theta\theta} = 0 \tag{B.2}$$

$$\sigma_{rr} = 0 \tag{B.3}$$

The in-plane equilibrium equations are rewritten with respect to cylindrical coordinate system as

$$\frac{\partial \sigma_{rr}}{\partial r} + \frac{1}{r}\frac{\partial \sigma_{r\theta}}{\partial \theta} + \frac{\sigma_{rr} - \sigma_{\theta\theta}}{r} = 0 \tag{B.4}$$

$$\frac{\partial \sigma_{r\theta}}{\partial r} + \frac{1}{r}\frac{\partial \sigma_{\theta\theta}}{\partial \theta} + \frac{2\sigma_{r\theta}}{r} = 0 \tag{B.5}$$

Substituting Eq. (B.1)–(B.3) into Eqs. (B.4) and (B.5) indicates that the in-plane equilibrium equations are satisfied. There is no stress discontinuity surface for the stress distribution due to M_z for the material elements near the nugget circumferential surface. Alternatively, the stresses for the material element bordering the nugget circumferential surface can be referred to the Cartesian coordinate system as

$$\sigma_{xx}^{M_z} = -\sigma_{r\theta}^{M_z} \sin 2\theta = \frac{2M_z}{\pi D^2 t} \sin 2\theta \tag{B.6}$$

$$\sigma_{yy}^{M_z} = \sigma_{r\theta}^{M_z} \sin 2\theta = -\frac{2M_z}{\pi D^2 t} \sin 2\theta \tag{B.7}$$

$$\sigma_{xy}^{M_z} = \sigma_{r\theta}^{M_z} \cos 2\theta = -\frac{2M_z}{\pi D^2 t} \cos 2\theta \tag{B.8}$$

With consideration of the twisting moment M_z, the stresses σ_{xx} and σ_{yy} in the four thin layers bordering the lower half nugget due to P_x, P_y and M_z as shown in Fig. 15 can be rewritten as

$$\sigma_{xx} = \sigma_{xx}^{P_x} + \sigma_{xx}^{M_z} = \mp\frac{P_x}{2Dt} + \frac{2M_z}{\pi D^2 t} \sin 2\theta \tag{B.9}$$

$$\sigma_{yy} = \sigma_{yy}^{P_y} + \sigma_{yy}^{M_z} = \mp\frac{P_y}{2Dt} - \frac{2M_z}{\pi D^2 t} \sin 2\theta \tag{B.10}$$

Now the normalized effective stress $\tilde{\tau}_e$ in Eq. (45) can be rewritten with consideration of the twisting moment M_z as

$$\begin{aligned}\tilde{\tau}_e^2 = {} & \frac{1}{3}\widetilde{P}_x^2 + \frac{1}{3}\widetilde{P}_y^2 - \frac{1}{3}\mathrm{sign}(\sigma_{xx}^{P_x})\mathrm{sign}(\sigma_{yy}^{P_y})\widetilde{P}_x\widetilde{P}_y - [\mathrm{sign}(\sigma_{xx}^{P_x})\widetilde{P}_x - \mathrm{sign}(\sigma_{yy}^{P_y})]\widetilde{P}_y\widetilde{M}_z \sin 2\theta + \widetilde{M}_z^2 \\ & + \left[\mathrm{sign}(\sigma_{xz}^{P_z})\alpha\widetilde{P}_z + \widetilde{P}_x\left(\frac{4t}{\pi D}\right) + 2\widetilde{M}_y\right]^2 + \left[\mathrm{sign}(\sigma_{yz}^{P_z})(1-\alpha)\widetilde{P}_z + \widetilde{P}_y\left(\frac{4t}{\pi D}\right) - 2\widetilde{M}_x\right]^2 = 1\end{aligned} \tag{B.11}$$

Here, $\mathrm{sign}(\sigma_{xx}^{P_x})$, $\mathrm{sign}(\sigma_{yy}^{P_y})$, $\mathrm{sign}(\sigma_{xz}^{P_z})$ and $\mathrm{sign}(\sigma_{yz}^{P_z})$ still represent the signs of corresponding stresses in each of the four regions as shown in Fig. 9. For a given monotonically increasing loading conditions when

the moment M_z is zero, the plastic collapse condition will be satisfied for the material element bordering the nugget circumferential surface in one, two or four of the four thin layers shown as dashed lines in Fig. 15, based on Eq. (B.11). For a given monotonically increasing loading conditions when the moment M_z is not zero, the yielding will first be satisfied at a material element bordering the nugget as one, two or four points in the four thin layers at $\theta = \pi/4$, $3\pi/4$, $5\pi/4$ or $7\pi/4$. However, the initial yielding at a specific point in a region cannot be considered as a plastic collapse of the region. Therefore, we cannot include the twisting moment into our limit load analysis. The inclusion of the twisting moment M_z is introduced empirically by including a quadratic term of $\overline{M}_z^2$ in the engineering failure criterion proposed in the main text based on the experimental results.

References

Anderson, T.L., 1995. Fracture Mechanics: Fundamentals and Applications. CRC Press Inc., Boca Raton, Florida.

Chao, Y., Miller, K., Wang, P.C., 1998. Impact strength of resistance spot welded joints. AWS Sheet Metal Welding Conference VIII, Detroit, Michigan, October 13–16, 1998, pp. 3–2.

Davidson, J.A., 1983. A review of the fatigue properties of spot-welded sheet steels. SAE Technical Paper No. 830033, Society of Automotive Engineers, Warrendale, Pennsylvania.

Ewing, K.W., Cheresh, M., Thompson, R., Kukuchek, P., 1982. Static and impact strengths of spot welded HSLA and low carbon steel joints. SAE Technical Paper No. 820281, Society of Automotive Engineers, Warrendale, Pennsylvania.

Hartmann, E.C., 1958. Mechanical tests of spot welds. Welding Journal 37, 520–523.

Lee, Y.-L., Wehner, T.J., Lu, M.-W., Morrissett, T.W., Pakalnins, E., 1998. Ultimate strength of resistance spot welds subjected to combined tension and shear. Journal of Testing and Evaluation 26, 213–219.

Lin, S.-H., Pan, J., Wu, S.-R., Tyan, T., 2001. Spot weld failure loads under combined mode loading conditions. SAE Technical Paper No. 2001-01-0428, Society of Automotive Engineers, Warrendale, Pennsylvania.

Lin, S.-H., Pan, J., Wu, S.-R., Tyan, T., Wung, P., 2002a. Failure loads of spot welds under combined opening and shear static loading conditions. International Journal of Solids and Structures 39, 19–39.

Lin, S.-H., Pan, J., Tyan, T., Wu, S.-R., Prasad, P., 2002b. Modeling and testing of spot welds under dynamic impact loading conditions. SAE Technical Paper No. 2002-01-0149, Society of Automotive Engineers, Warrendale, Pennsylvania.

Lin, S.-H., Pan, J., Wu, S.-R., Tyan, T., Prasad, P., 2003. Failure loads of spot-weld specimens under impact opening and shear loading conditions, in press, Experimental Mechanics.

Lin, P.-C., Lin, S.-H., Pan, J. A finite element analysis for spot welds under dominated shear loading conditions, submitted for publication.

Merkle, J.G., Corten, H.T., 1974. *J* integral analysis for the compact specimen, considering axial force as well as bending effects. Journal of Pressure Vessel Technology 96, 286–292.

Pan, J., 1984. Some considerations on estimation of energy release rates for circumferentially cracked pipes. ASME Journal of Pressure Vessel Technology 106, 391–398.

Pan, J., 1986. Estimation of energy release rates and instability analysis for a pipe with a circumferential surface crack subjected to bending. ASME Journal of Pressure Vessel Technology 108, 33–40.

Peterson, W., Borchelt, J., 2000. Maximizing cross tension impact properties of spot welds in 1.5 mm low carbon, dual-phase and martensitic steels. SAE Technical Paper No. 2001-01-2680, Society of Automotive Engineers, Warrendale, Pennsylvania.

Radaj, D., 1989. Stress singularity, notch stress and structural stress at spot-welded joints. Engineering Fracture Mechanics 34, 495–506.

Sawhill, J.M., Furr, S.T., 1981. Spot weldibility tests for high-strength steels. SAE Technical Paper No. 810352, Society of Automotive Engineers, Warrendale, Pennsylvania.

Sheppard, S.D., Pan, N., 2001. A look at fatigue: is resistance spot welds-notch or crack? SAE Technical Paper No. 2001-01-0433, Society of Automotive Engineers, Warrendale, Pennsylvania.

Swellam, M.H., Banas, G., Lawrence, F.V., 1994. A fatigue design parameter for spot welds. Fatigue and Fracture of Engineering Materials and Structures 17, 1197–1204.

Thornton, P., Krause, A., Davies, R., 1996. Aluminum spot weld. Welding Journal 75, 101–108.

VandenBossche, D.J., 1977. Ultimate strength and failure mode of spot welds in high strength steels. SAE Technical Paper No. 770214, Society of Automotive Engineers, Warrendale, Pennsylvania.

Wang, P.-C., Ewing, K.W., 1991. Fracture mechanics analysis of fatigue resistance of spot welded coach-peel joints. Fatigue and Fracture of Engineering Materials and Structures 14, 913–930.

Wung, P., 2001a. A force-based failure criterion for spot weld analysis. Journal of Experimental Mechanics 41, 107–113.

Wung, P., 2001b. A method for spot welded structure analysis. SAE Technical Paper No. 2001-01-0427, Society of Automotive Engineers, Warrendale, Pennsylvania.

Wung, P., Walsh, T., Ourchane, A., Stewart, W., Jie, M., 2001. Failure of spot welds under in-plane static loading. Journal of Experimental Mechanics 41, 100–106.

Zhang, S., 2001. Recent developments in analysis and testing of spot welds. SAE Technical Paper No. 2001-01-0432, Society of Automotive Engineers, Warrendale, Pennsylvania.

Zuniga, S., Sheppard, S.D., 1995. Determining the constitutive properties of the heat-affected zone in a resistance spot weld. Modeling and Simulation in Materials Science and Engineering 3, 391–416.

Zuniga, S., Sheppard, S.D., 1997. Resistance spot weld failure loads and modes in overload conditions. In: Piascik, R.S., Newman, J.C., Dowling, N.E. (Eds.), Fatigue and Fracture Mechanics, ASTM STP 1296. American Society for Testing and Materials, pp. 469–489.